Handling complex source structures in global EM induction studies: from C-responses to new arrays of transfer functions

Puethe, Christoph; Kuvshinov, Alexey; Olsen, Nils

Published in:
Geophysical Journal International

Link to article, DOI:
10.1093/gji/ggv021

Publication date:
2015

Document Version
Publisher's PDF, also known as Version of record

Geophysical Journal International

Geophys. J. Int. (2015) **201,** 318–328 doi: 10.1093/gji/ggv021

GJI Geomagnetism, rock magnetism and palaeomagnetism

Handling complex source structures in global EM induction studies: from *C*-responses to new arrays of transfer functions

Christoph Püthe,[1] Alexey Kuvshinov[1] and Nils Olsen[2]

[1]*Institute of Geophysics, ETH Zürich, Sonneggstrasse 5, CH-8092 Zürich, Switzerland. E-mail: christoph.puethe@erdw.ethz.ch*

[2]*DTU Space, Technical University of Denmark, Diplomvej 371, DK-2800 Kongens, Lyngby, Denmark*

Accepted 2015 January 12. Received 2014 October 27; in original form 2014 April 16

SUMMARY

The *C*-response is a conventional transfer function in global electromagnetic induction research and is traditionally determined from observations of magnetic variations in the vertical and horizontal components. Its interpretation relies on the assumption that the source of the variations is well approximated by a large-scale symmetric (magnetospheric) ring current, described by a single spherical harmonic. However, there is growing evidence for a more complex structure of this source. In this paper, we investigate the variability of *C*-responses due to sources different from the dominating large-scale symmetric ring current. We show that the effect is significant and persists at all periods. Describing the magnetospheric source by a single spherical harmonic coefficient thus injects substantial errors into the estimated responses. To overcome the problem, we introduce arrays of alternative transfer functions that relate the components of the magnetic variation to different spherical harmonic coefficients. These transfer functions can handle a complex spatial structure of the magnetospheric source. Compared to *C*-responses, we observe a significant increase in the coherencies relating input and output quantities of the new transfer functions, especially at high latitudes. This increases the usability of observatory magnetic data for the recovery of global 3-D mantle conductivity structure.

Key words: Time-series analysis; Geomagnetic induction; Magnetic and electrical properties.

1 INTRODUCTION

Transfer functions are mathematical representations of the relations between input and output signals of a system in the frequency domain (Girod *et al.* 2001). By means of these functions, it is possible to determine the response of a system to a specified source. Transfer functions are independent of the amplitude of the source, which makes their use advantageous in many applications. The term is often exclusively assigned to linear systems, for which the determination of transfer functions is simplified.

Due to the linearity of Maxwell's equations, the conducting Earth itself can be seen as a linear system. The use of transfer functions is common in electromagnetic (EM) sounding research, although a separation of input signals (EM fields due to primary, extraneous currents) and output signals (EM fields due to secondary, induced currents) is usually difficult, as measured EM fields contain contributions of both. Under certain assumptions and by means of mathematical transformations, it is however often possible to estimate transfer functions directly from relations between measured field components.

A classical example of such a transfer function is the *C*-response (Schmucker 1970), which can be used to sense the 1-D conductivity structure beneath the site for which it was determined. The *C*-response is widely applicable and intuitively understood, as its real part corresponds to the centre depth of the induced currents and thereby is indicative of the depth to which EM fields (of a given period) can penetrate (Weidelt 1972).

At periods considered in global induction studies, the *C*-response is conveniently determined with the Z/H method (Banks 1969). This method relates the vertical and horizontal components of the magnetic variation at a specific site, hence only requires measurements from a single location. But it relies on prior knowledge about the spatial structure of the inducing source, namely that the latter only has a single degree of freedom. The Z/H method was, for example applied by Schultz & Larsen (1987) and Khan *et al.* (2011) to observatory magnetic data in order to determine local 1-D conductivity profiles. Both studies relied on the assumption that the source can be described by a zonal harmonic of degree 1 (so-called P_1^0 assumption).

Thanks to recent improvements in global 3-D EM forward modelling algorithms and the growth of computational resources, rigorous 3-D inversions for mantle conductivity have come into reach. The first large-scale regional (e.g. Koyama *et al.* 2006; Shimizu *et al.* 2010; Koyama *et al.* 2014) and global (e.g. Kelbert *et al.*

2009; Semenov & Kuvshinov 2012) studies revealed a heterogeneous structure of mid-mantle conductivity. These studies are based on C-responses estimated with the Z/H method from magnetic data taken by the global network of geomagnetic observatories—and thus also on the P_1^0 assumption.

However, there has long been evidence for a more complex structure and asymmetry of the magnetospheric ring current (e.g. Daglis & Kozyra 2002; Balasis *et al.* 2004; Olsen & Kuvshinov 2004; Balasis & Egbert 2006). The recovered conductivity structures, both in 1-D and 3-D studies, might thus be contaminated by errors originating from an inaccurate description of the source.

In this study, we seek for a solution to the problems associated with the Z/H method. To this purpose, we first systematically investigate the global variability of C-responses estimated with the Z/H method due to a more realistic structure of the magnetospheric source, which includes spherical harmonic terms up to degree 3. This gives us an idea of the error injected into C-responses estimated under the P_1^0 assumption.

We then introduce sets of alternative transfer functions, which relate the components of the magnetic variation at the measuring site to different spherical harmonic expansion (SHE) coefficients describing the magnetospheric source. These transfer functions are thus able to deal with a more complex spatial structure of the source.

The paper is organized as follows. In Section 2, we review the concept of EM transfer functions, introduce the C-response and squared coherencies. In Section 3, we present modelling results and demonstrate the variability of C-responses due to complexities in the source structure. Sets of alternative transfer functions are introduced in Section 4. In Section 5, we determine these transfer functions from observatory data and compare their coherencies to those of corresponding C-responses. How the alternative transfer functions could be used in the context of an inversion for global 3-D mantle conductivity is discussed in Section 6. Appendices A and B summarize the computations underlying the results presented in Section 3.

2 EM TRANSFER FUNCTIONS

2.1 The magnetic potential

EM fields obey Maxwell's equations. We formulate them in the frequency domain as

$$\frac{1}{\mu_0}\nabla\times\mathbf{B}=\sigma\mathbf{E}+\mathbf{j}^{\text{ext}}, \tag{1}$$

$$\nabla\times\mathbf{E}=\mathrm{i}\omega\mathbf{B}. \tag{2}$$

Here $\mathbf{B}(\mathbf{r},\omega)$ and $\mathbf{E}(\mathbf{r},\omega)$ are the complex Fourier transforms of magnetic flux density and electric field, respectively, and $\mathbf{j}^{\text{ext}}(\mathbf{r},\omega)$ is the complex Fourier transform of the electric current density of the inducing source. The position vector $\mathbf{r}=(r,\vartheta,\varphi)$ describes a spherical coordinate system (oriented with the geomagnetic dipole), with r, ϑ and φ being distance from Earth's centre, colatitude and longitude, respectively. Further, $\sigma(\mathbf{r})$ is the spatial conductivity distribution in the Earth, ω denotes angular frequency and μ_0 is the magnetic permeability of free space. Our formulation of Maxwell's equations discards displacement currents, which are negligible in the considered frequency range (<1 Hz). Note that we adopt the Fourier convention

$$f(t)=\frac{1}{2\pi}\int_{-\infty}^{\infty}f(\omega)\,\mathrm{e}^{-\mathrm{i}\omega t}\,\mathrm{d}\omega. \tag{3}$$

Just above Earth's surface and in the electrically insulating atmosphere, eq. (1) reduces to $\nabla\times\mathbf{B}=0$ due to vanishing conductivity and absence of source currents. $\mathbf{B}$ is thus a potential field and can be written as the gradient of a scalar magnetic potential V, that is $\mathbf{B}=-\nabla V$. Since $\mathbf{B}$ is solenoidal, V satisfies Laplace's equation, $\nabla^2V=0$. The solution can be represented as sum of external and internal parts (e.g. Backus *et al.* 1996), $V=V^{\text{ext}}+V^{\text{int}}$, with

$$V^{\text{ext}}(\mathbf{r},\omega)=a\sum_{n=1}^{\infty}\sum_{m=-n}^{n}\varepsilon_n^m(\omega)\left(\frac{r}{a}\right)^n Y_n^m(\vartheta,\varphi), \tag{4}$$

$$V^{\text{int}}(\mathbf{r},\omega)=a\sum_{k=1}^{\infty}\sum_{l=-k}^{k}\iota_k^l(\omega)\left(\frac{a}{r}\right)^{(k+1)} Y_k^l(\vartheta,\varphi). \tag{5}$$

Here a is Earth's mean radius, and $\varepsilon_n^m(\omega)$ and $\iota_k^l(\omega)$ are the SHE coefficients of the external (inducing) and internal (induced) parts of the potential, respectively. Y_n^m is the spherical harmonic of degree n and order m,

$$Y_n^m(\vartheta,\varphi)=P_n^{|m|}(\cos\vartheta)\,\mathrm{e}^{\mathrm{i}m\varphi}, \tag{6}$$

with $P_n^{|m|}(\cos\vartheta)$ being the associated Legendre functions. In particular, $Y_1^0=P_1^0=\cos\vartheta$ is the zonal harmonic of degree 1, which can be used to describe the magnetic field due to a large-scale symmetric ring current around the geomagnetic equator. Note that we in the following adopt the convention

$$\sum_{n,m}=\sum_{n=1}^{\infty}\sum_{m=-n}^{n}. \tag{7}$$

2.2 Sources and transfer functions

Eqs (1) and (2) reflect that electric and magnetic fields are linear with respect to the source. Because of this, there must also be a linear relation between the internal part of the potential V^{int} (i.e. the 'output' of the conducting Earth) and the external part V^{ext} (i.e. its 'input'). Following the notation of Egbert & Booker (1989), we thus can write

$$V^{\text{int}}(\mathbf{r}_a,\omega)=\mathbf{L}_\omega[V^{\text{ext}}(\mathbf{r}_a,\omega)], \tag{8}$$

where $\mathbf{r}_a=(a,\vartheta,\varphi)$ describes Earth's surface. The linear operator $\mathbf{L}_\omega$ depends on frequency and on the conductivity structure. We will now illustrate the concept with a simple example. In case of a 1-D Earth and a source described by a single spherical harmonic, let us take Y_1^0, the double sums in eqs (4) and (5) collapse, and we obtain

$$V^{\text{ext}}(\mathbf{r}_a,\omega)=a\varepsilon_1^0(\omega)Y_1^0(\vartheta,\varphi), \tag{9}$$

$$V^{\text{int}}(\mathbf{r}_a,\omega)=a\iota_1^0(\omega)Y_1^0(\vartheta,\varphi). \tag{10}$$

Cancelling terms reveals that the linear operator $\mathbf{L}_\omega$ is in this case nothing but the scalar Q-response of degree 1,

$$\iota_1^0(\omega)=Q_1(\omega)\varepsilon_1^0(\omega). \tag{11}$$

In general, $\mathbf{L}_\omega$ contains all information about electrical conductivity in the Earth that can be obtained from measurements on its surface (Egbert & Booker 1989). The ultimate goal of EM studies must thus be to obtain as much information as possible about this operator. However, apart from very simple examples as the one above, a unique and complete determination of $\mathbf{L}_\omega$ is not possible. This is mostly due to limited spatial and spectral data coverage, and associated with this, the difficulty to separate external and internal parts of the potential, as only their superposition is measured.

For a more practical treatment of the problem, Egbert & Booker (1989) introduced the 'response space'. This concept is based on the assumption that the source can be described by p independent spatial modes, or, in other words, that the space of source potentials has p degrees of freedom. In this case, it is possible to introduce linear mappings relating one (output) observable and any p input observables, as demonstrated in detail by Egbert & Booker (1989). The linear mappings are the intercomponent and interstation transfer functions applied in practice in EM induction research. For example, in magnetotellurics (MT) the source is represented by $p = 2$ plane waves of different polarizations. A set of widely used transfer functions are the elements of the so-called tipper, which relate the vertical component of the magnetic field with its $p = 2$ horizontal components.

2.3 P_1^0 assumption and C-response

At long periods (days to months) usually considered in global induction, most studies assume that the source of EM variations is a magnetospheric ring current, which can be described by a single spatial mode in the form of a zonal spherical harmonic of degree 1 (so-called P_1^0 assumption). Hence, $p = 1$, implying the existence of transfer functions connecting any two field components. The long periods impede the use of electric data. As apparent from eq. (2), the electric field vanishes as frequency decreases. Moreover, $Y = B_\varphi = 0$ in a 1-D Earth excited by a P_1^0-source, such that it is of little use for induction studies (although a transfer function involving Y was proposed by Fujii & Schultz (2002) to detect lateral conductivity heterogeneities).

It is thus natural to devise a transfer function connecting $Z = -B_r$ and $X = -B_\vartheta$. This was first done by Banks (1969) and later on referred to as Z/H method (as the horizontal magnetic variation H equals X under the given assumptions). By means of a simple scaling, this transfer function becomes equivalent to the C-response (Schmucker 1970; Weidelt 1972), which is then given by

$$C(\mathbf{r}_a, \omega) = -\frac{a \tan\vartheta}{2} \frac{B_r(\mathbf{r}_a, \omega)}{B_\vartheta(\mathbf{r}_a, \omega)} = -\frac{a \tan\vartheta}{2} \frac{Z(\mathbf{r}_a, \omega)}{X(\mathbf{r}_a, \omega)}. \quad (12)$$

In contrast to the Q-response (eq. 11), which reflects the globally laterally averaged conductivity, the C-response can be used to sense the 1-D conductivity profile at a specific location. It is easily shown that C-responses are the same everywhere on the surface of a 1-D Earth. In other words, spatial variations of C-responses estimated with the Z/H method reflect either conductivity heterogeneities or a violation of the P_1^0 assumption. We will discuss this issue in Section 3.

2.4 The concept of coherencies

In a noise-free system excited by a source with p degrees of freedom, a given field component is perfectly described by a linear combination of p other field components. In practice, we can test the assumption of a p-dimensional source field by measuring the correlation between the given 'output' field component and the p 'inputs'. In time-series analysis, the squares of correlation coefficients are frequently denoted as squared coherencies (e.g. Bendat & Piersol 2010). Ordinary squared coherencies measure the correlation between the output and a the ith input ($i = 1...p$), while multiple squared coherencies measure the correlation of the output with a linear combination of all inputs. We will apply this concept in the forthcoming sections.

High coherencies do not necessarily prevent from a misinterpretation of the estimated transfer functions. Even if the value of p is correctly estimated, we do not know the spatial structure of the source. Moreover, the coherencies of scalar transfer functions such as the C-response do not carry information about the dimensionality of the conductivity structure. In other words, even a C-response with coherency approaching 1 might be biased by local conductivity heterogeneities, and interpreting it for a 1-D structure will necessarily lead to an erroneous model.

3 VARIABILITY OF C-RESPONSES

3.1 Observed variability

We now investigate the variability of C-responses determined under the P_1^0 assumption. We first estimate C-responses from 16 yr of observatory data (1997–2012) with the Z/H method. The results for 77 observatories, located at geomagnetic latitudes between $\pm 10^\circ$ and $\pm 55^\circ$, are shown in Fig. 1. If the source was described perfectly by the first zonal harmonic and if conductivity depended only on depth, the derived C-responses at a given frequency should be the same everywhere at Earth's surface (indicated by the solid black lines). However, Fig. 1 reveals a huge variability both in the real and the imaginary part of C at all periods.

The top panel of Fig. 1 shows squared coherencies between Z and X for all observatories. Average coherencies (of all observatories) increase from <0.5 at short periods to a maximum of 0.7 at a period of 32 d. Hence, a significant proportion of the variations in Z cannot be explained by variations in X. This challenges the assumption of $p = 1$.

For clarity of presentation, we do not show uncertainties of C-response estimates in Fig. 1. As a measure of the uncertainties, which vary strongly among different observatories, we use the 90 per cent confidence interval (e.g. Aster *et al.* 2005). The mean of the confidence interval (at all observatories) increases from about 100 km at a period of 2 d to about 180 km at a period of 32 d. It is thus in this period range considerably smaller than the overall variability of both real and imaginary part of C (*cf.* Fig. 1). For longer periods, the mean of the confidence interval clearly exceeds 200 km

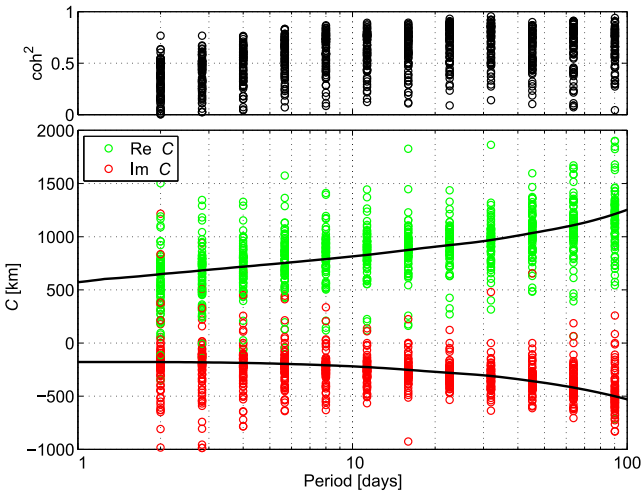

Figure 1. Variability of observed C-responses, estimated at 77 mid-latitude observatories with the Z/H method from 16 yr of observatory data (1997–2012). The solid lines indicate the theoretical prediction, corresponding to the 1-D conductivity profile derived from satellite data by Kuvshinov & Olsen (2006). The top panel shows squared coherencies.

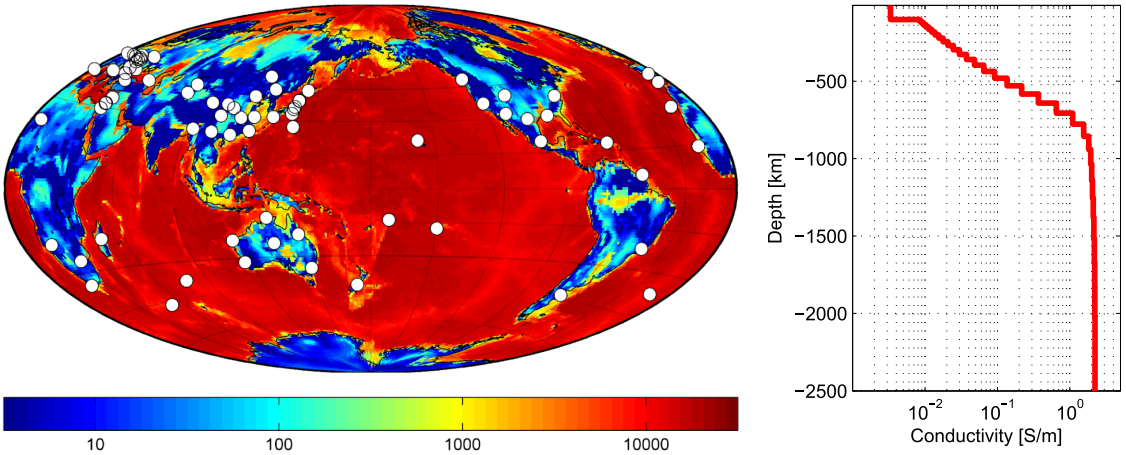

Figure 2. 3-D conductivity model. Left-hand panel: surface conductance (in S), representing the uppermost 10 km. White dots indicate the locations of geomagnetic observatories for which *C*-responses were estimated (*cf.* Fig. 1) and of which data were used to determine the SHE of the magnetospheric source. Right-hand panel: 1-D conductivity profile beneath the surface shell.

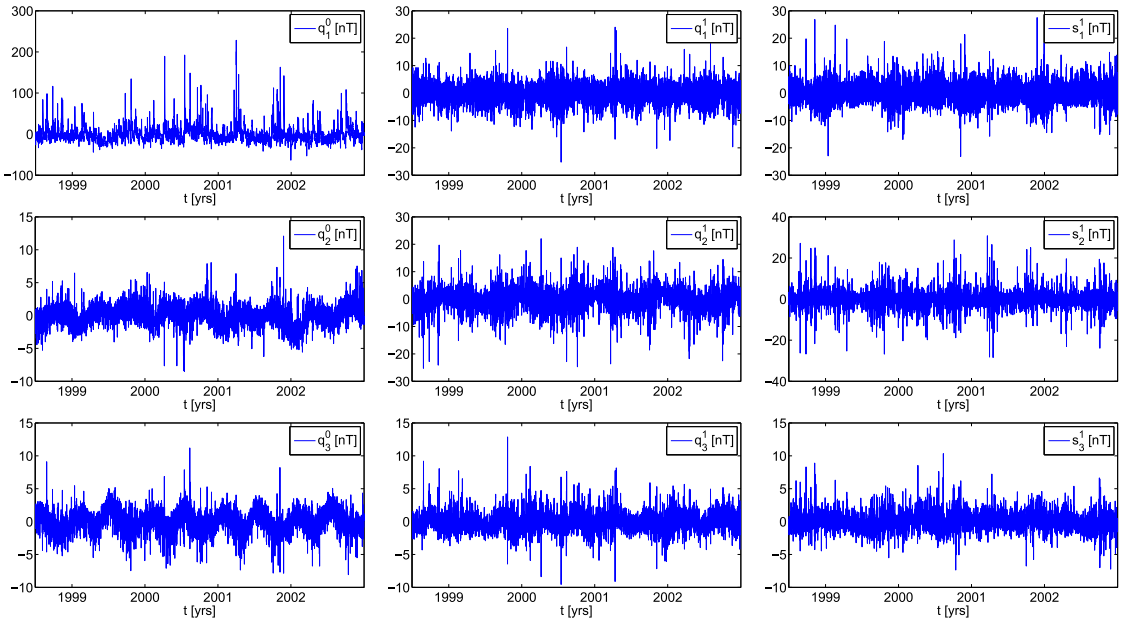

Figure 3. Time-series of the external coefficients q_n^m, s_n^m (in nT) that describe the source in our model study. Ticks indicate January 1 of the respective years. Note that the real coefficients $q_n^m(t)$, $s_n^m(t)$ shown in this figure are related to the complex coefficients $\varepsilon_n^m(t)$ in the following way: $\varepsilon_n^m = (q_n^m - \mathrm{i}s_n^m)/2$ if $m > 0$, $\varepsilon_n^m = (q_n^{|m|} + \mathrm{i}s_n^{|m|})/2$ if $m < 0$, and $\varepsilon_n^0 = q_n^0$. Also note the different scales of the individual plots.

and becomes comparable to the overall variability. Hence, a part of the observed variability might be explained by measurement uncertainties. However, particularly for periods <32 d, the variability is too large to be explained solely by (uncorrelated) noise in the data.

3.2 Numerical modelling

In order to analyse the origin of the observed variability, we tried to reproduce the pattern shown in Fig. 1 numerically. To this purpose, we computed Z/H *C*-responses from synthetic magnetic data obtained by simulating induction due to a realistic source (including higher degree terms ε_n^m in addition to ε_1^0) in a 3-D conductivity model. The chosen conductivity model consists of a thin, laterally heterogeneous surface shell (with a resolution of $1^\circ \times 1^\circ$), mainly representing the distribution of conductive oceans and resistive continents (surface shell model taken from Manoj *et al.* 2006), and a layered model underneath, recovered from satellite magnetic data by Kuvshinov & Olsen (2006). The conductivity model is depicted in Fig. 2. In order to separately investigate the effects of source and conductivity structure, we also investigate induction in the corresponding 1-D model (i.e. the conductivity profile shown in the right part of Fig. 2 without the surface shell).

The realistic source is described by external coefficients ε_n^m of the SHE of the magnetic field due to signals of magnetospheric origin. Hourly mean time-series of these coefficients in a geomagnetic dipole coordinate system (up to degree $n = 3$ and order $m = 1$) were obtained by analysis of 16 years of observatory data (1997–2012) with the method described in Appendix A. For the computation of synthetic *C*-responses, we used subsets of 4.5 yr of these time-series (1998 July–2002 December), which are depicted in Fig. 3.

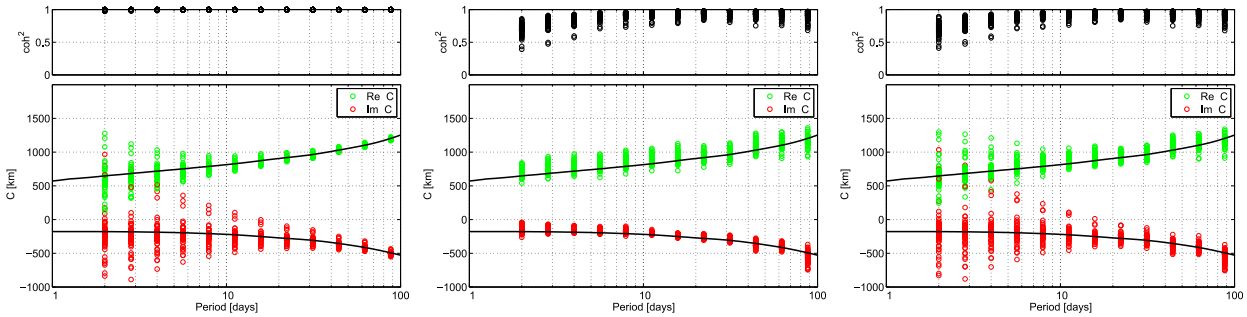

Figure 4. Variability of modelled C-responses for the locations of 77 observatories at geomagnetic latitudes between $\pm 10^\circ$ and $\pm 55^\circ$. Left-hand panel: variability due to the ocean effect (case b). Middle panel: variability due to a complex source (case c). Right-hand panel: variability due to ocean and source effect (case d). The black lines in all plots denote, as a reference, the globally uniform C-response corresponding to the 1-D model that has been excited by ε_1^0 (case a).

For our analysis we generated synthetic data sets for each of the following four cases:

(a) Induction due to a simplified source (only coefficient ε_1^0) in the 1-D model.

(b) Induction due to a simplified source (only coefficient ε_1^0) in the 3-D model. With this case we study the influence of the 'ocean effect'.

(c) Induction due to a complex source (described by nonzero coefficients ε_n^m, $n \leq 3$, $|m| \leq 1$) in the 1-D model. With this case we study the influence of the 'source effect'.

(d) Induction due to a complex source in the 3-D model. This case contains both ocean effect and source effect.

The procedure to estimate C-responses is the same for each of the four cases. Details are provided in Appendix B.

Fig. 4 presents the squared coherency, $\mathrm{coh}^2(C)$, between Z and X and the estimated C-responses for the simulated cases (b)–(d). Shown are results for the 77 observatories at geomagnetic latitudes between $\pm 10^\circ$ and $\pm 55^\circ$ of Fig. 1. Outside this latitude range, the estimation of C-responses with the Z/H method becomes unstable, that is already minor violations of the assumptions can lead to large errors. This becomes apparent when analysing eq. (12): At the equator ($\vartheta = 90^\circ$), a vanishing Z must compensate for $\tan\vartheta$ approaching infinity, while at the poles ($\vartheta = 0^\circ$, resp. 180°), a vanishing H must compensate for $\tan\vartheta$ approaching zero.

The left-hand panel of Fig. 4 shows results obtained by simulating induction due to ε_1^0 in the given 3-D model (case b). It thus presents the variability of C-responses due to the ocean effect. The variability is very large for short periods, spanning more than 1000 km at a period of 2 d. As expected, it decreases with increasing period, since longer periods sample deeper regions of the Earth and are thus less affected by heterogeneities in the top layer. The variability of C-responses due to the ocean effect is discussed in detail by Semenov & Kuvshinov (2012). The coherency is equal to one, because $p = 1$ is fulfilled and there is no noise in the synthetic data.

The middle panel of Fig. 4 shows results obtained by simulating induction due to the full set of spherical harmonic sources in the corresponding 1-D model. It thus presents the variability of the responses due to source structures other than Y_1^0 (case c). The real part of the responses (Re C) seems to be slightly more affected than the imaginary part (Im C). A variability in Re C of about 500 km is apparent for virtually the entire period range. For periods >10 d, the variability of Re C due to source effects becomes dominant over the variability due to the ocean effect. For Im C, the source effect variability dominates over the ocean effect variability only at periods >40 d. Interestingly, the source effect variability of Im C is minimum at a period of 12 d. On average, the source effect variability comprises about 50 per cent of the responses themselves.

The right panel of Fig. 4 shows results obtained by simulating induction due to the full set of spherical harmonic sources in the 3-D model (case d). With this simulation, we want to mimic the situation on Earth. The synthetic C-responses show a large variability, explaining a major part of the variability seen in the observed C-responses (*cf.* Fig. 1). Low coherency indicates that the output variable Z cannot fully be described by the input variable H and thus confirms that $p \neq 1$. This is an example of correlated noise due to undescribed sources (e.g. Egbert & Booker 1989). Coherencies are however still substantially larger than for observed C-responses, indicating that there are more sources of noise than derived by us.

Spatial patterns of both source and ocean effect can be analysed by plotting global maps of C-responses, as presented in Fig. 5. We show the real and imaginary part for three selected periods (2.0, 13.6 and 91.3 d). The panels of Fig. 5 correspond to the cases (a)–(d) presented above. As a reference, Fig. 5(a) shows the C-responses computed in a 1-D model that was excited by ε_1^0. As expected, the responses are the same everywhere on the globe. Fig. 5(b) presents C-responses corresponding to induction due to the same source (ε_1^0) in a 3-D model. The remaining columns show C-responses corresponding to induction due to the full set of source terms in a 1-D model (c) and a 3-D model (d), respectively.

The effect of a complex source structure is presented in Fig. 5(c). It is most clearly seen at the period of 91.3 d. As expected and already discussed, maximum anomalies in C-responses are detected in polar and equatorial regions (defined by geomagnetic latitude). But anomalous C-responses are also very pronounced in mid-latitudes. For example, Im C shows a strong source effect in the Indian Ocean. Another prominent feature follows the geometry of the geomagnetic equator. The effect can be traced up to geomagnetic latitudes of $\pm 20^\circ$, which in particular means that C-responses at many mid-latitude observatories (for example Honolulu) are likely influenced by the source complexity.

Fig. 5(d) also contains the estimated C-responses at observatory locations as coloured dots. Modellings and estimates are in good agreement at a period of 2.0 d, but deviate strongly at 91.3 d. This is likely due to the large uncertainties of C-response estimates at long periods.

A comparison of the results presented in Figs 5(b), (c) and (d) confirms that the ocean effect is the dominant source of variability for short periods, while the source effect dominates at long periods. The imaginary part at long periods is more affected by the ocean effect than the real part. Ocean effect and source effect together can explain a large proportion of the variability seen in observatory

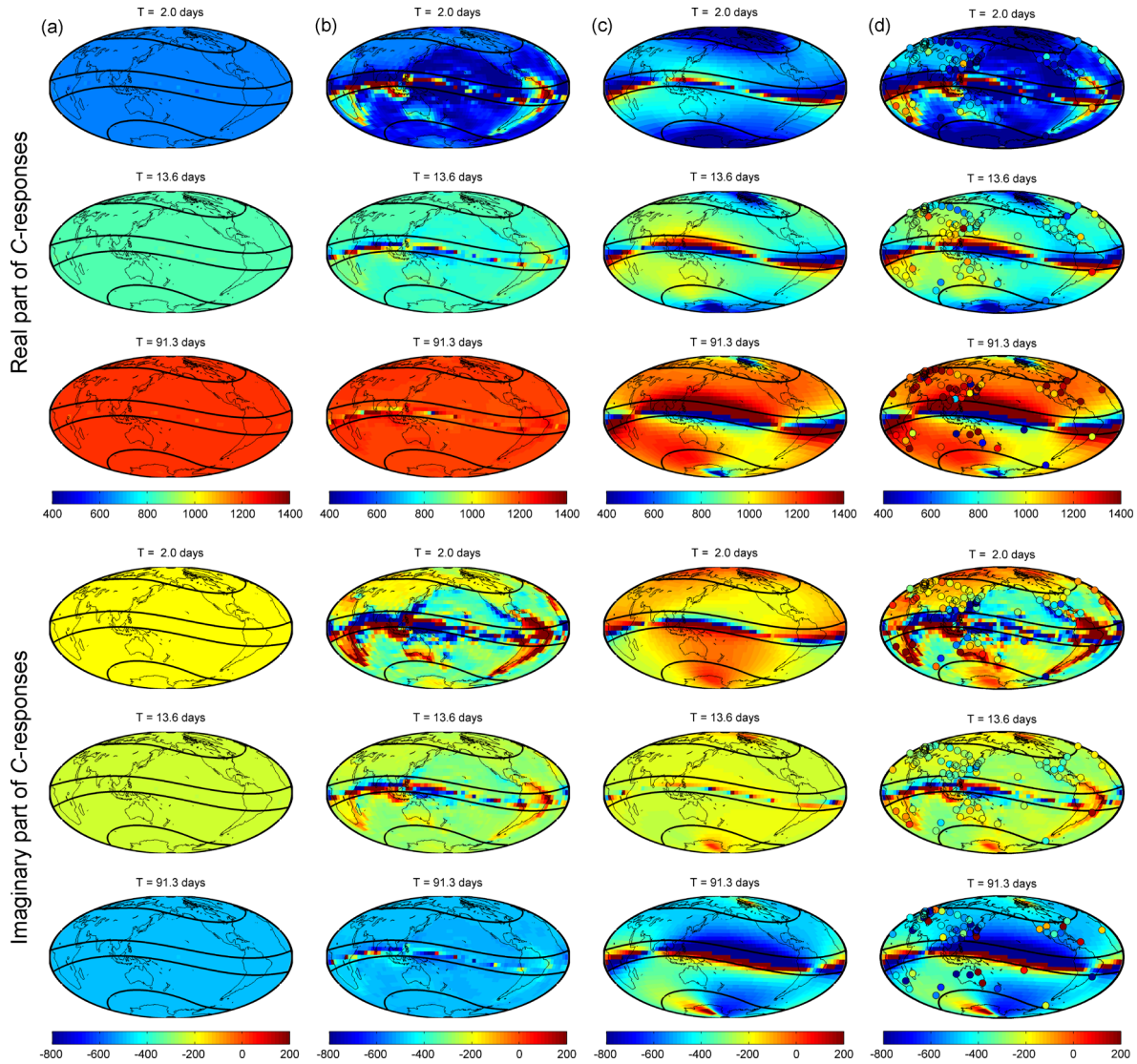

Figure 5. Maps of modelled *C*-responses (in km) for periods of 2.0, 13.6 and 91.3 d, respectively. Top panels: real part, bottom panels: imaginary part of *C*. (a) 1-D model, excited by ε_1^0. (b) 3-D model, excited by ε_1^0 (showing the ocean effect). (c) 1-D model, excited by the full set of ε_n^m (showing the source effect). (d) 3-D model, excited by the full set of ε_n^m (showing ocean and source effects). The solid black lines indicate geomagnetic latitudes of $\pm 10^\circ$ and $\pm 55^\circ$, respectively. Observed responses at observatory locations are added as coloured dots to panel (d).

C-responses. Differences between observed and computed responses might be due to erroneous data, more complicated source structures (e.g. the auroral electrojet, *cf.* Semenov & Kuvshinov 2012) and deep 3-D conductivity heterogeneities.

4 INTRODUCING NEW TRANSFER FUNCTIONS

Based on the results of the previous section, we now want to formulate criteria a transfer function should fulfil to be useful for induction studies. We will see that, by design, the *C*-response can only fulfil a part of these criteria. We will therefore seek for alternatives to overcome the shortcomings associated with *C*-responses.

An ideal transfer function must show high coherencies between its input and output channels to ensure that all sources have been taken into account. It should be highly sensitive to induction processes. For generality, it should be applicable in 3-D environments, and 3-D structures should be apparent in the estimated transfer function.

Which of these criteria does the *C*-response fulfil? Since its estimation with the Z/H-method involves the Z-component of magnetic variations, the *C*-response is highly sensitive to induction processes. For the same reason, it is however also sensitive to conductivity heterogeneities, which can, as seen in the previous section, lead to enormous biases in the estimates. Whether the subsurface is 1-D, 2-D or 3-D is usually not readily apparent in *C*-responses, just like in other scalar transfer functions. Further, if the *C*-response is estimated with the Z/H-method, it is based on the assumption that $p = 1$. As shown above, the presence of other sources leads to dropping coherencies, which can make a reliable interpretation of the estimated transfer function in terms of conductivity impossible.

In MT, the impedance tensor has many of the desired properties. It thus seems natural to also devise arrays of transfer functions for global induction studies. A consistent treatment can be envisioned by a 3-D modification of eq. (11), which reads

$$\iota_k^l(\omega) = \sum_{n,m} Q_{kn}^{lm}(\omega)\varepsilon_n^m(\omega). \tag{13}$$

Q_{kn}^{lm} is a 2-D array of transfer functions that we refer to as 'Q-matrix' and that was, for example discussed by Olsen (1999). Estimation of the Q-matrix, its analysis and interpretation have been described by Püthe & Kuvshinov (2014). In practice, an estimation of the Q-matrix however hinges on the precise determination of induced fields in a spherical harmonic representation. This is difficult to accomplish in a 3-D Earth with a sparse network of irregularly distributed observatories.

We will now devise transfer functions that combine advantages of both Q-matrix and C-response. Thanks to the linearity of Maxwell's equations with respect to the source, the magnetic field can be represented as the sum of individual magnetic fields due to specific sources. Using a spherical harmonic parametrization of the source, we can thus write the magnetic field outside the source region as

$$\mathbf{B}(\mathbf{r},\omega)=\sum_{n,m}\varepsilon_n^m(\omega)\mathbf{B}_n^m(\mathbf{r},\omega). \tag{14}$$

$\mathbf{B}_n^m(\mathbf{r},\omega)$ is the magnetic field due to a unit scale spherical harmonic source. In particular, we can write for $Z=-B_r$

$$Z(\mathbf{r},\omega)=\sum_{n,m}\varepsilon_n^m(\omega)T_n^m(\mathbf{r},\omega). \tag{15}$$

$T_n^m(\mathbf{r},\omega)$ can be regarded as a transfer function relating the Z-component of the magnetic variation at the measuring site to the source coefficient $\varepsilon_n^m(\omega)$. The T_n^m form a 1-D, potentially infinite array. In practice, its size is limited by the number of external SHE coefficients that can be determined.

Eq. (14) also holds in regions in which $\nabla\times\mathbf{B}\neq 0$, for example under water. Therefore, transfer functions T_n^m can also be estimated for ocean bottom stations. For ground-based magnetic observatories ($r=a$), the T_n^m are easily related to the Q-matrix as

$$T_n^m(\mathbf{r}_a,\omega)=nY_n^m(\vartheta,\varphi)-\sum_{k,l}(k+1)Q_{kn}^{lm}(\omega)Y_k^l(\vartheta,\varphi), \tag{16}$$

which is easily verified from eqs (4), (5), (13) and (14). In contrast to the Q-matrix, the T_n^m make use of local information on the conductivity structure and are thus suitable transfer functions in case of sparse and irregularly distributed observations.

The above equations are in particular also valid if the source can be described by the single spherical harmonic Y_1^0 alone and conductivity only depends on depth. T_1^0 is in this case related to the C- and Q-responses,

$$T_1^0(\vartheta,\omega)=\frac{3C(\omega)}{a+C(\omega)}\cos\vartheta=[1-2Q_1(\omega)]\cos\vartheta. \tag{17}$$

In the zero-order-approximation $|C|\ll a$ in the considered period range; therefore, T_1^0 is roughly proportional to C. We can expect a similarity in shape even if ε_1^0 is not the only, but the dominating source coefficient. In contrast to C, all T_n^m vary with geographical location by definition. Note also that while estimating C is a univariate problem, estimating the T_n^m is generally a multivariate problem.

For the horizontal components of the magnetic variation, $X=-B_\vartheta$ and $Y=B_\varphi$, we can analogously define

$$X(\mathbf{r},\omega)=\sum_{n,m}\varepsilon_n^m(\omega)U_n^m(\mathbf{r},\omega) \tag{18}$$

and

$$Y(\mathbf{r},\omega)=\sum_{n,m}\varepsilon_n^m(\omega)V_n^m(\mathbf{r},\omega). \tag{19}$$

In case of ground-based magnetic observations, U_n^m and V_n^m relate to the Q-matrix as

$$U_n^m(\mathbf{r}_a,\omega)=\frac{\partial Y_n^m(\vartheta,\varphi)}{\partial\vartheta}+\sum_{k,l}Q_{kn}^{lm}(\omega)\frac{\partial Y_k^l(\vartheta,\varphi)}{\partial\vartheta} \tag{20}$$

and

$$V_n^m(\mathbf{r}_a,\omega)=-\frac{\mathrm{i}}{\sin\vartheta}\left[mY_n^m(\vartheta,\varphi)+\sum_{k,l}lQ_{kn}^{lm}(\omega)Y_k^l(\vartheta,\varphi)\right]. \tag{21}$$

We want to note that we mainly introduced U_n^m and V_n^m for completeness. In practice, these transfer functions do not prove very beneficial for a recovery of the conductivity structure. Since they only involve the horizontal components of the magnetic variation, U_n^m and V_n^m are not very sensitive to induction processes. We will thus in the following mainly focus on transfer functions T_n^m.

5 APPLICATION TO OBSERVATORY DATA

5.1 Description of the source

The concept elaborated in the previous section is now applied to observatory hourly mean values of the years 1997–2012. To derive time-series of external coefficients ε_n^m ($n\leq 3$, $m\leq 1$), we applied the method described in Appendix A. Note that these are the same coefficients as used previously in Section 3, just that the time-series were cropped to 4.5 yr for numerical modelling in order to speed up computations.

Power spectra of the coefficients are shown in Fig. 6. Clear peaks are visible at 1 d and its harmonics, reflecting the daily Sq variations—with, as expected, most energy in coefficient ε_2^1. Further distinct peaks are apparent at 1 yr (and its second harmonic), with most energy in coefficient ε_2^0. Both daily and yearly variations are of ionospheric origin and are known to be due to a complicated source. We are however interested in periods between 1 and 100 d, in which magnetic variations are mostly of magnetospheric origin. In this period range, coefficient ε_1^0 has most energy, as apparent from Fig. 6. The dominance of ε_1^0 increases with period; for periods >10 d, other coefficients seem to be negligible. However, as seen in Section 3, these appearances are deceiving.

5.2 Observatory transfer functions

From time-series of ε_n^m, X, Y and Z, we estimated, according to eqs (15)–(21), the proposed transfer functions T_n^m, U_n^m and V_n^m for selected observatories. To this purpose, we used the multivariate time-series analysis algorithm recently presented by Püthe & Kuvshinov (2014). The algorithm is based on the section-averaging method and iteratively re-weighted least squares (e.g. Aster *et al.* 2005). Uncertainties were estimated with a jackknife approach (e.g. Chave & Thomson 1989). As a reference, we also estimated C-responses with the Z/H method.

In Fig. 7, we present estimates of C and T_n^m for the observatory Hermanus (HER, South Africa, geomagnetic latitude 34°S). As expected, C and T_1^0 are similar in shape. This similarity confirms that ε_1^0 is the dominant inducing coefficient. However, T_n^m of higher n and $|m|$ are non-zero and show distinct structures (especially at short periods), for example T_3^0, T_2^{-1} and T_2^1. The uncertainties of these responses increase at periods >30 d, which is probably due to the limited length of the time-series. In solid lines, we show modelled transfer functions corresponding to the conductivity model of Fig. 2.

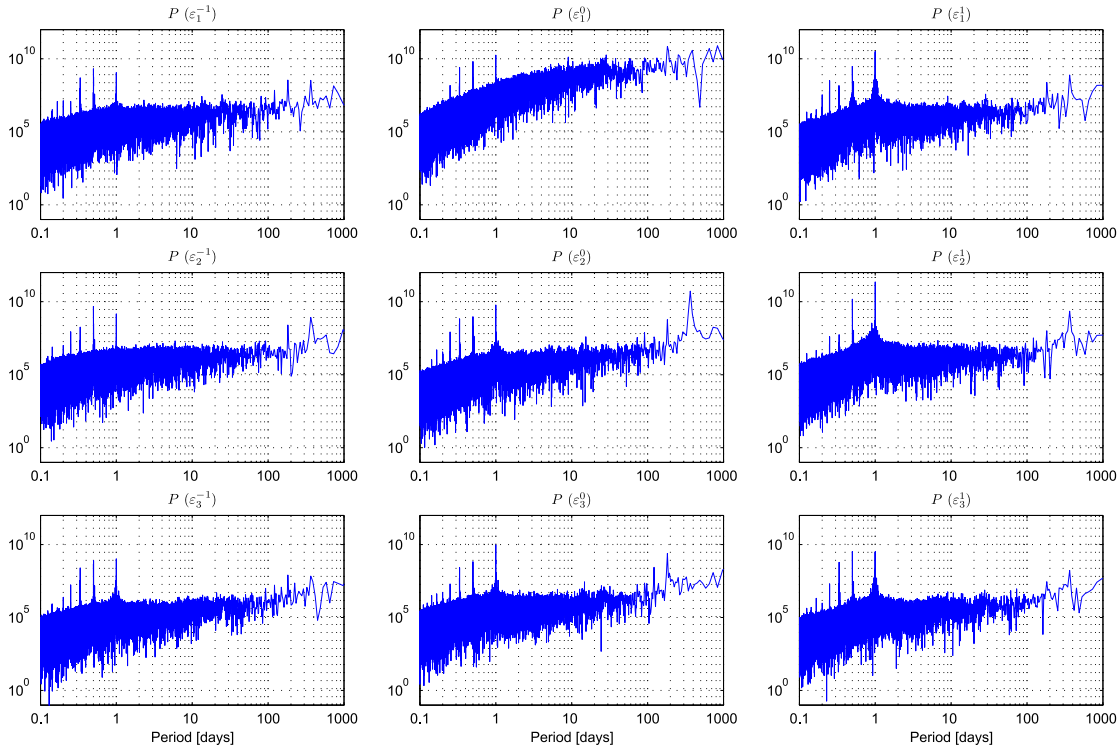

Figure 6. Power spectral density of the external coefficients ε_n^m (in nT^2), here defined as $P[\varepsilon_n^m(\omega)] = |\varepsilon_n^m(\omega)|^2$.

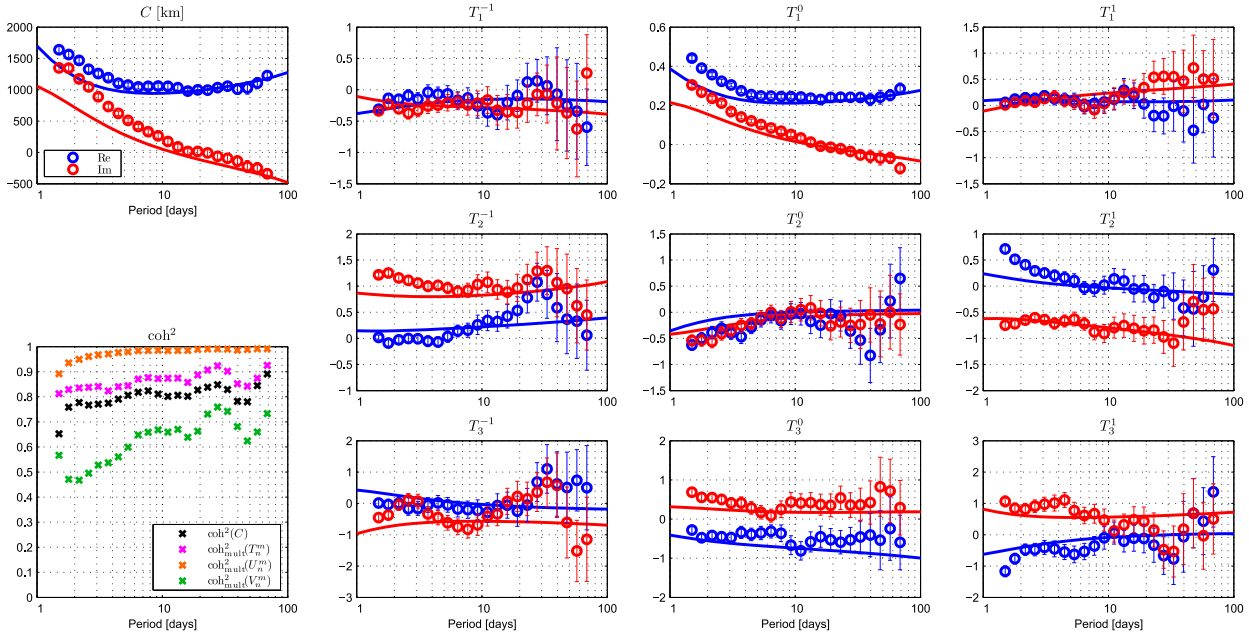

Figure 7. Transfer functions estimated for the observatory Hermanus (HER, South Africa) at geomagnetic latitude of 34°S. The top panel in the first column shows C-responses. The bottom panel in the first column shows squared coherencies for C and multiple squared coherencies for the alternative transfer functions T_n^m, U_n^m and V_n^m. The further panels show the transfer functions T_n^m ($n \leq 3$, $m \leq 1$). For all responses, the real part is presented in blue, the imaginary part in red. The 90 per cent confidence interval is indicated for each estimate. Modelled transfer functions, corresponding to the conductivity model shown in Fig. 2, are marked by solid lines.

For many T_n^m, there is a good correspondence between estimates and modellings, at least concerning the general trend. Differences might be due to noise in the data, inaccuracies in the estimated source coefficients, but also due to structures not present in our simplified conductivity model. The latter is probably the reason for the differences between modelled and estimated T_1^0 at periods <5 d.

We do not show transfer functions U_n^m and V_n^m for the reasons mentioned in Section 4—both are not very sensitive to induction.

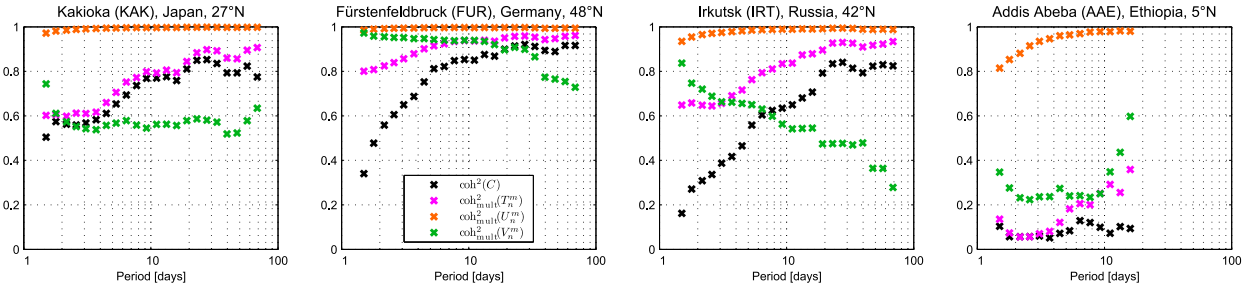

Figure 8. Squared coherencies for C (black) and multiple squared coherencies for T_n^m (magenta), U_n^m (orange) and V_n^m (green) at different geomagnetic observatories. Geomagnetic latitude is indicated.

However, analysing their coherencies can help to understand the source structure. Squared coherencies $\mathrm{coh}^2(C)$ and multiple squared coherencies $\mathrm{coh}^2_{\mathrm{mult}}(T_n^m)$, $\mathrm{coh}^2_{\mathrm{mult}}(U_n^m)$ and $\mathrm{coh}^2_{\mathrm{mult}}(V_n^m)$ are presented in the bottom left-hand panel of Fig. 7. The plot clearly shows that for all periods, $\mathrm{coh}^2_{\mathrm{mult}}(T_n^m) > \mathrm{coh}^2(C)$. This means that the addition of a small number of source terms substantially increases the coherency and thus decreases the bias of the estimated responses by correlated noise (in agreement with the results of Olsen 1998).

Squared coherencies for the V_n^m are relatively small; indeed, $\mathrm{coh}^2_{\mathrm{mult}}(V_n^m) < \mathrm{coh}^2(C)$ for all periods. The low coherencies primarily indicate that variations of Y at HER cannot be explained by low-degree spherical harmonic sources alone. In contrast, $\mathrm{coh}^2_{\mathrm{mult}}(U_n^m)$ are very large and approach 1 with increasing period. Variations in X at HER are thus well explained by low-degree spherical harmonic sources. Note that, when deriving the ε_n^m by a spherical harmonic analysis (SHA) of the horizontal components of **B**, we excluded data from HER to avoid any circularity in our analysis. Tests however showed that this has only very minor effects on the resulting transfer functions and coherencies. The effect might be larger for more isolated observatories (e.g. Honolulu).

We do not show ordinary coherencies for individual T_n^m, U_n^m and V_n^m, describing the proportion of Z, X or Y, respectively, that can be described by the individual inputs ε_n^m. The ordinary coherency for T_1^0 is very similar to that of the C-response. The coherencies for other T_n^m are small (generally below 0.2), but non-zero and thus contribute to $\mathrm{coh}^2_{\mathrm{mult}}$. The ordinary coherency for U_1^0 approaches unity for periods longer than 5 days. In contrast to Z, variations in X are thus well explained by a large-scale symmetric ring current. Coherencies for other U_n^m are low. Among the V_n^m, V_1^0, V_2^{-1} and V_2^1 show the highest ordinary coherencies (ranging between 0.2 and 0.4, depending on period).

5.3 Analysis of coherencies

For further locations, we focus on the squared coherencies. Fig. 8 shows coherency plots for the observatories Kakioka (KAK, Japan), Fürstenfeldbruck (FUR, Germany), Irkutsk (IRT, Russia) and Addis Abeba (AAE, Ethiopia).

For the mid-latitude observatory KAK, the addition of source terms does not lead to a substantial increase in the coherencies, that is $\mathrm{coh}^2_{\mathrm{mult}}(T_n^m) \approx \mathrm{coh}^2(C)$ at all periods. For FUR and IRT, coh^2 however increases substantially when estimating the T_n^m instead of C, especially at short periods. We have mentioned in Section 3 that the estimation of C-responses with the Z/H method becomes unstable towards high latitudes. The addition of source terms other than ε_1^0 seems to improve the situation. The low coherencies of C at FUR and IRT are however not only due to the way C is estimated. The measurements at both observatories are believed to be influenced by the polar electrojet (e.g. Fujii & Schultz 2002; Semenov & Kuvshinov 2012). The transfer functions of higher n and $|m|$ might thus 'catch' part of the noise arising from this source.

Coherencies of C are generally very low for AAE. This is due to the vanishing Z-component close to the geomagnetic equator, as discussed in Section 3. $\mathrm{coh}^2_{\mathrm{mult}}(T_n^m)$ are not much larger, indicating that the chosen subset of ε_n^m can not explain the variations of Z at AAE.

For KAK, FUR and IRT, coherencies of C, T_n^m and U_n^m increase with period. We attribute this behaviour to a growing dominance of ε_1^0 at longer periods. This assumption is confirmed by the power spectra shown in Fig. 6. The same argument holds for the decrease of $\mathrm{coh}^2_{\mathrm{mult}}(V_n^m)$ with increasing period, since a source described spatially by Y_1^0 does not contribute to variations in Y unless conductivity heterogeneities are present.

Multiple squared coherencies of the U_n^m are very high for all observatories analysed in this study. This is even the case at AAE, where the other transfer functions fail. The high coherencies of U_n^m are due to the fact that the X-component of magnetic variations only vanishes near the poles and is less sensitive to source structures of high n than the Z-component (*cf.* eqs A1–A3).

In this study, we assumed that the source can be described by 9 external SHE coefficients ($p = 9$). Compared to the usual assumption of $p = 1$, we observed a substantial increase in coherencies, especially at periods <10 d and geomagnetic latitudes $>40^\circ$. The choice of coefficients however was rather arbitrary and does not have a physical basis. Adding more source terms might permit an even better agreement between input and output. However, ε_n^m of even higher n and $|m|$ are hard to determine accurately. Moreover, there is a trade-off between the number of input source terms (i.e. ε_n^m) and the period range for which transfer functions can be determined, as discussed by Püthe & Kuvshinov (2014).

6 CONCEPT OF AN INVERSION

Semenov & Kuvshinov (2012) inverted C-responses of the global network of geomagnetic observatories for 3-D mantle conductivity structure. The alternative transfer functions T_n^m introduced in this study could be inverted in a similar fashion. If treated with care, U_n^m (and potentially also V_n^m) might be useful in regions where coherencies of T_n^m are small, particularly near the equator. While Semenov & Kuvshinov (2012) excluded observatories at low and high latitudes from their analysis, we could, with a suitable combination of T_n^m, U_n^m and V_n^m, use data from these observatories, permitting a better global coverage.

Our modular inversion code (Püthe & Kuvshinov 2014) is easily modified to incorporate new data types. Modifications mainly concern a new formulation of the data misfit and the adjoint source,

which is used to compute the misfit gradient. Following the general methodology presented by Pankratov & Kuvshinov (2010), such a formulation is also straightforward. We applied the required modifications and successfully tested the inversion code with synthetic data.

The main difference to the inversion of *C*-responses however is the requirement for time-series of the external SHE coefficients ε_n^m. In this study, an SHA of the measured horizontal components of the magnetic variation was performed to estimate the *unseparated* coefficients v_n^m (*cf.* eqs A2–A3). External and internal contributions were subsequently separated by using the conductivity model shown in Fig. 2. In the context of an inversion, this strategy appears to be rather tautologic. One possible solution is to simultaneously determine source and conductivity structure in a looped sequential procedure, as recently discussed by Koch & Kuvshinov (2013).

The main result of Section 5, the substantial increase in coherencies, is independent of the conductivity model used to separate internal and external contributions. Therefore, the fact that our model does not perfectly describe Earth's conductivity structure does not affect the validity of the results in this study.

An iterative approach could be avoided by relating unseparated coefficients v_n^m, rather than ε_n^m, to Z. This would essentially be equivalent to the $Z/\mathcal{Y}$ method (Schmucker 1979; Olsen 1998). A recovery of v_n^m is always possible without using prior information about the conductivity structure. The $Z/\mathcal{Y}$ method however suffers from the intrinsic assumption that not only the source, but also the conductivity, only varies on large spatial scales.

Due to the sparse and irregular distribution of observatories, we do not plan to recover a 3-D mantle conductivity model from ground-based data alone, but rather use the transfer function T_n^m (possibly together with U_n^m and V_n^m) as additional constraints on the solution when inverting satellite data (e.g. Q-matrices, *cf.* Püthe & Kuvshinov 2014). Such an inversion is planned with data provided by the *Swarm* multisatellite mission.

7 CONCLUSIONS

It is well-known that the *C*-responses estimated at geomagnetic observatories around the globe with the classical Z/H method show a large variability. The Z/H method relies on the assumptions of a source exclusively described by Y_1^0 and 1-D conductivity. We have demonstrated in this study that the variability is not only due to conductivity heterogeneities. Components of the magnetospheric source other than Y_1^0 cause a substantial variability, which persists at all periods between a few days and a few months.

An alternative set of transfer functions, relating the *Z*-component of magnetic variations to external SHE coefficients, has been introduced to overcome this problem. With observatory data, it has been shown that considering nine low-degree external coefficients instead of a single one substantially increases the coherency between inputs (time-series of SHE coefficients ε_n^m) and output (time-series of the local *Z*-component). This is in particular the case at high latitudes, where the polar electrojet is believed to affect the measurements. With a more suitable parametrization of the source, which describes its main characteristics with as few terms as possible, even higher coherencies might be attainable. Deriving such a parametrization is a challenge we want to tackle in the future.

The concept elaborated in this paper could easily be extended to other types of data, such as measurements of the tangential components of the electric field, voltage data from abandoned submarine telecommunication cables or sea-bottom magnetic signals. In combination with satellite data, the alternative transfer functions can be used to recover the 3-D conductivity structure of Earth's mantle.

ACKNOWLEDGEMENTS

The authors thank the staff of the geomagnetic observatories for collecting and distributing the magnetic data used in this study. We extend our gratitude to Takao Koyama and an anonymous reviewer for constructive comments on the manuscript. This work has been supported by the Swiss National Science Foundation under grant No. 2000021-140711/1 and in part by the Russian Foundation for Basic Research under grant No. 12-05-00817-a.

REFERENCES

Aster, R., Borchers, B. & Thurber, C., 2005. *Parameter Estimation and Inverse Problems,* Elsevier Academic Press.

Backus, G., Parker, R. & Constable, C., 1996. *Foundations of Geomagnetism,* Cambridge Univ. Press.

Balasis, G. & Egbert, G., 2006. Empirical orthogonal function analysis of magnetic observatory data: further evidence for non-axisymmetric magnetospheric sources for satellite induction studies, *Geophys. Res. Lett.,* **33,** doi:10.1029/2006GL025721.

Balasis, G., Egbert, G. & Maus, S., 2004. Local time effects in satellite estimates of electromagnetic induction transfer functions, *Geophys. Res. Lett.,* **31,** doi:10.1029/2004GL020147.

Banks, R., 1969. Geomagnetic variations and the electrical conductivity of the upper mantle, *Geophys. J. R. astr. Soc.,* **17,** 457–487.

Bendat, J. & Piersol, A., 2010. *Random Data. Analysis and Measurement Procedures,* 4th edn, John Wiley & Sons.

Chave, A. & Thomson, D., 1989. Some comments on magnetotelluric response function estimation, *J. geophys. Res.,* **94,** 14 215–14 225.

Daglis, I. & Kozyra, J., 2002. Outstanding issues of ring current dynamics, *J. Atmos. Sol. Terr. Phys.,* **64,** 253–264.

Egbert, G. & Booker, J., 1989. Multivariate analysis of geomagnetic array data. 1. The response space, *J. geophys. Res.,* **94,** 14 227–14 247.

Fujii, I. & Schultz, A., 2002. The 3-D electromagnetic response of the Earth to the ring current and auroral oval excitation, *Geophys. J. Int.,* **151,** 689–709.

Girod, B., Rabenstein, R. & Stenger, A., 2001. *Signals and Systems,* Wiley.

Kelbert, A., Schultz, A. & Egbert, G., 2009. Global electromagnetic induction constraints on transition-zone water content variations, *Nature,* **460,** 1003–1007.

Khan, A., Kuvshinov, A. & Semenov, A., 2011. On the heterogeneous electrical conductivity structure of the Earth's mantle with implications for transition zone water content, *J. geophys. Res.,* **116,** doi:10.1029/2010JB007458.

Koch, S. & Kuvshinov, A., 2013. Global 3-D EM inversion of Sq variations based on simultaneous source and conductivity determination: concept validation and resolution studies, *Geophys. J. Int.,* **195,** 98–116.

Koyama, T., Shimizu, H., Utada, H., Ichiki, M., Ohtani, E. & Hae, R., 2006. Water content in the mantle transition zone beneath the North Pacific derived from the electrical conductivity anomaly, in *Earth's Deep Water Cycle,* Vol. 168, pp. 171–179, eds Jacobsen, S. & van der Lee, S., AGU Geophys. Monogr. Ser.

Koyama, T., Khan, A. & Kuvshinov, A., 2014. Three-dimensional electrical conductivity structure beneath Australia from inversion of geomagnetic observatory data: evidence for lateral variations in transition-zone temperature, water content and melt, *Geophys. J. Int.,* **196,** 1330–1350.

Kuvshinov, A., 2008. 3-D global induction in the oceans and solid Earth: recent progress in modeling magnetic and electric fields from sources of magnetospheric, ionospheric and oceanic origin, *Surv Geophys,* **29,** 139–186.

Kuvshinov, A. & Olsen, N., 2006. A global model of mantle conductivity derived from 5 years of CHAMP, Ørsted, and SAC-C magnetic data, *Geophys. Res. Lett.,* **33,** doi:10.1029/2006GL027083.

Manoj, C., Kuvshinov, A., Maus, S. & Lühr, H., 2006. Ocean circulation generated magnetic signals, *Earth Planets Space,* **58,** 429–437.
Olsen, N., 1998. The electrical conductivity of the mantle beneath Europe derived from *C*-responses from 3 to 720 hr, *Geophys. J. Int.,* **133,** 298–308.
Olsen, N., 1999. Long-period (30 days – 1 year) electromagnetic sounding and the electrical conductivity of the lower mantle beneath Europe, *Geophys. J. Int.,* **138,** 179–187.
Olsen, N. & Kuvshinov, A., 2004. Modeling the ocean effect of geomagnetic storms, *Earth Planets Space,* **56,** 525–530.
Pankratov, O. & Kuvshinov, A., 2010. General formalism for the efficient calculation of derivatives of EM frequency domain responses and derivatives of the misfit, *Geophys. J. Int.,* **181,** 229–249.
Pankratov, O., Avdeev, D. & Kuvshinov, A., 1995. Electromagnetic field scattering in a heterogeneous Earth: a solution to the forward problem, *Phys. Solid Earth,* **31,** 201–209.
Püthe, C. & Kuvshinov, A., 2014. Mapping 3-D mantle electrical conductivity from space: a new 3-D inversion scheme based on analysis of matrix *Q*-responses, *Geophys. J. Int.,* **197,** 768–784.
Schmucker, U., 1970. *Anomalies of Geomagnetic Variations in the Southwestern United States,* Vol. 13: Bull. Scripps Inst. Ocean., Univ. Calif.
Schmucker, U., 1979. Erdmagnetische Variationen und die elektrische Leitfähigkeit in tieferen Schichten der Erde, *Sitzungsbericht und Mitteilungen Braunschweigische Wiss. Gesellschaft,* **4,** 45–102.
Schultz, A. & Larsen, J.C., 1987. On the electrical conductivity of the mid-mantle – I. Calculation of equivalent scalar magnetotelluric response functions, *Geophys. J. Int.,* **88,** 733–761.
Semenov, A. & Kuvshinov, A., 2012. Global 3-D imaging of mantle conductivity based on inversion of observatory *C*-responses – II. Data analysis and results, *Geophys. J. Int.,* **191,** 965–992.
Shimizu, H., Utada, H., Baba, K., Koyama, T., Obayashi, M. & Fukao, Y., 2010. Three-dimensional imaging of electrical conductivity in the mantle transition zone beneath the North Pacific Ocean by a semi-global induction study, *Phys. Earth planet. Int.,* **183,** 262–269.
Weidelt, P., 1972. The inverse problem of geomagnetic induction, *Z. Geophys.,* **38,** 257–289.

APPENDIX A: RECOVERY OF SOURCE COEFFICIENTS

At the surface of the Earth, the magnetic field vector components are derived by taking the negative gradient of the magnetic potential given by eqs (4) and (5) and setting $\mathbf{r} = \mathbf{r}_a$. This yields

$$B_r(\mathbf{r}_a, \omega) = -\sum_{n,m} z_n^m(\omega) Y_n^m(\vartheta, \varphi), \tag{A1}$$

$$B_\vartheta(\mathbf{r}_a, \omega) = -\sum_{n,m} v_n^m(\omega) \frac{\partial Y_n^m(\vartheta, \varphi)}{\partial \vartheta}, \tag{A2}$$

$$B_\varphi(\mathbf{r}_a, \omega) = -\sum_{n,m} v_n^m(\omega) \frac{1}{\sin\vartheta} \frac{\partial Y_n^m(\vartheta, \varphi)}{\partial \varphi}, \tag{A3}$$

with $v_n^m = \varepsilon_n^m + \iota_n^m$ and $z_n^m = n\varepsilon_n^m - (n+1)\iota_n^m$. In vector notation, the time domain equivalents of eqs (A2) and (A3) can be combined to

$$\mathbf{B}_\tau(\mathbf{r}_a, t) = -\sum_{n,m} v_n^m(t) \nabla_\perp Y_n^m(\vartheta, \varphi), \tag{A4}$$

where subscript τ denotes the horizontal part of $\mathbf{B}$ and $\nabla_\perp$ is the angular part of the gradient operator.

Our method to recover external SHE coefficients ε_n^m requires a conductivity model of the Earth (Fig. 2) and involves the following steps.

(i) Simulation of EM induction due to unit amplitude spherical harmonic sources $\varepsilon_n^m = 1$ in frequency domain at a set of logarithmically spaced frequencies ω_j. To this purpose, we use a numerical solution (Kuvshinov 2008) based on a contracting integral equation approach (Pankratov *et al.* 1995). The calculations yield responses to unit scale spherical harmonic sources at Earth's surface, termed $\mathbf{B}_n^m(\mathbf{r}_a, \omega_j)$.

(ii) Calculation of scalar Q-responses $Q_n(\omega_j)$ from the $\mathbf{B}_n^m(\mathbf{r}_a, \omega_j)$ by using eq. (31) of Püthe & Kuvshinov (2014).

(iii) Collection of magnetic data from all available observatories at mid-latitudes and removal of core and crustal field by fitting the data with a low-degree polynomial.

(iv) Using the horizontal components of these data, construction of a system of linear equations (A4) and solution of this system for unseparated coefficients v_n^m. This is done separately for each instant t.

(v) Fourier transformation of the unseparated coefficients, yielding $v_n^m(\omega)$.

(vi) Spectral interpolation of Q_n to the full set of frequencies contained in the data.

(vii) Separation of external and internal contributions with the formula $\varepsilon_n^m(\omega) = v_n^m(\omega)/[1 + Q_n(\omega)]$, which follows from eq. (11).

(viii) If required, time-series of ε_n^m are obtained by inverse Fourier transform.

A different method, which completely works in frequency domain and incorporates 3-D effects in a more consistent way, was presented by Olsen & Kuvshinov (2004). That method is however only applicable if there are no gaps in the data. We found in a different context that both methods yield very similar source models, thus justifying our simplified technique for this study.

APPENDIX B: CALCULATION OF SYNTHETIC *C*-RESPONSES

Given the $\mathbf{B}_n^m(\mathbf{r}_a, \omega_j)$ and time spectra of coefficients ε_n^m, both obtained with the methods described in Appendix A, synthetic *C*-responses at sites of interest $\mathbf{r}_s$ can be calculated in the following way.

(i) Spatial interpolation of the $\mathbf{B}_n^m(\mathbf{r}_a, \omega_j)$ to sites of interest, yielding $\mathbf{B}_n^m(\mathbf{r}_s, \omega_j)$.

(ii) Spectral interpolation of $\mathbf{B}_n^m$ to the full set of frequencies contained in the data, yielding $\mathbf{B}_n^m(\mathbf{r}_s, \omega)$.

(iii) Computation of magnetic field time spectra at site $\mathbf{r}_s$ by exploiting the linearity of Maxwell's equations with respect to the source, that is

$$\mathbf{B}(\mathbf{r}_s, \omega) = \sum_{n,m} \varepsilon_n^m(\omega) \mathbf{B}_n^m(\mathbf{r}_s, \omega). \tag{B1}$$

(iv) Inverse Fourier transformation, yielding time-series $\mathbf{B}(\mathbf{r}_s, t)$.

(v) Estimation of *C*-responses from time-series of B_r and B_ϑ with the Z/H-method, *cf.* eq. (12). This is done with a univariate data analysis algorithm, using the section-averaging method (e.g. Olsen 1998) and iteratively re-weighted least squares (e.g. Aster *et al.* 2005).

Note that the components of $\mathbf{B}_n^m$ are essentially equivalent to the new transfer functions T_n^m, U_n^m and V_n^m introduced in Section 4 of this study.